A computational framework for predicting the fracture toughness of metals as function of microstructure

Ushasi Roy, Min Zhou*

The George W. Woodruff School of Mechanical Engineering, School of Materials Science and Engineering, Georgia Institute of Technology, Atlanta, Georgia, 30332-0405, USA

ABSTRACT

We present a simplified computational framework based on the cohesive finite element method (CFEM) for predicting the macroscale fracture measures such as K_{IC} and J_{IC} of ductile metals as functions of microstructural attributes. Currently, no systematic approach exists to explicitly quantify the effects of grain and grain boundary behavior on the fracture measures of polycrystalline materials. Our computational approach involves embedding a microstructure region around the crack tip in a compact tension specimen subjected to mode-I loading and explicitly resolving fracture processes in the microstructure. To track how the interplay between intergranular and transgranular fracture mechanisms affect the fracture processes and consequently K_{IC} and J_{IC}, a grain boundary misorientation dependent interfacial separation model is used. The framework allows exploration of the effects of microstructure on the macroscopic fracture measures via the manifestation of different fracture mechanisms. Calculations carried out for Mo capture and delineate the competing effects between (a) intergranular and transgranular fracture and (b) constituent plasticity and fracture on the overall fracture toughness of the material. The use of statistically equivalent microstructure sample sets (SEMSS) allows the statistical distributions of K_{IC} to be predicted for Mo with different grain sizes. The results indicate that, as the minimum grain boundary interfacial strength decreases and the grain yield strength increases, intergranular fracture becomes more pronounced over transgranular fracture. Consequently, the plastic dissipation primarily associated with transgranular fracture is suppressed, resulting in lower overall fracture toughness. Microstructures with intermediate levels of grain size exhibit the toughest material response via a combination of tortuous crack paths and plastic dissipation. Finally, the results are analytically quantified in a manner that takes into account the effects of grain boundary characteristics, constituent plasticity, and stochasticity via the use of the SEMSS. Although the calculations here are performed on Mo in a simplified setting, the approach can be extended and applied to other material systems.

© 2020 Elsevier Ltd. All rights reserved.

1. Introduction

Designing new materials with microstructures for tailored properties requires studies that allow the exploration of the correlation between macroscale properties and microstructural attributes. Mechanical responses at the macroscale are governed by material microstructural characteristics at lower scales and their evolution under loading. The fracture behavior is

one prime example. Extensive studies have been carried out on ways to enhance material behavior through microstructure design (Fullwood et al., 2010; Liu et al., 2015; McDowell and Olson, 2008; Olson, 1997) in the last few decades. The fracture toughness of brittle materials such as ceramics and composites have been quantitatively correlated with microstructure by accounting micromechanisms of crack propagation (Chen et al., 2015; Ebrahimi et al., 2019; Hossain et al., 2014; Li and Zhou, 2013a, b; Prakash et al., 2016). For polycrystalline ductile materials, less has been done towards explicitly tracking crack paths and quantitatively capturing their influence on the overall fracture toughness (Li et al., 2014; Li and Zhou, 2018; Osovski et al., 2019; Prakash et al., 2016; Srivastava et al., 2017). In Liu et al., 2019; Srivastava et al., 2017; Srivastava et al., 2014; Tvergaard and Needleman, 2006, ductile fracture is modeled via void nucleation and growth associated with inclusions or second phase particles using modified Gurson's models (Gurson, 1977; Pardoen and Hutchinson, 2000). The polycrystalline grain structure is not explicitly modeled. In Zikry, 1992; Zikry and Kameda, 1998; Zikry and Kao, 1995, crack propagation paths are modeled as a function of the grain boundary characteristics in bicrystals. Polycrystalline grain structures are considered in Guo et al., 2012; Osovski et al., 2015, in analyses of intergranular crack propagation in β-Ti alloys. In Chen et al., 2015 nonlocal lattice particle model is used to study microstructural effects on fracture of polycrystalline aggregates. The results show that the intergranular crack propagation acts as a toughening mechanism and the ductile crack growth resistance is dependent on crack paths in a manner similar to brittle crack growth resistance. Osovski et al., 2019 analyzed the potential of crack path engineering in polycrystalline ductile materials. Molkeri et al., 2019 analyzed the intergranular crack growth resistance as a function of the grain size. Musienko et al., 2007 analyzed intergranular fracture in the context of corrosion.

Experimental studies (Kobayashi et al., 2008; Lim and Watanabe, 1989; Lim and Watanabe, 1990; Watanabe, 1993, 1994) on grain boundary (GB) engineering of metals and alloys show that GB types and characteristics such as misorientation angle heavily influence fracture behavior. For example, Arafin and Szpunar, 2010 studied the intergranular fracture susceptibility as a function of grain boundary character distribution in Mo. Bachurin, 2018 qualitatively correlated crack paths in polycrystalline Pd with the GB misorientation. Despite these studies, quantitative relations between the mechanisms and fracture toughness are non-existent, and the effects have not been systematically accounted for in models, including the models mentioned above. Furthermore, experiments show that fracture surfaces of ductile materials almost always involve a combination of intergranular and transgranular crack propagation, but only a few attempts (Bond and Zikry, 2018; Li et al., 2014; Li and Zhou, 2018; Prakash et al., 2016) have been made to capture the interplay between intergranular and transgranular crack paths. In particular, Li and Zhou, 2018 studied the competition between intergranular and transgranular crack propagation and the competition between deformation and fracture in an AZ31 Mg alloy. The model assumes uniform GB properties and does not account for the effects of the misorientation angle. Bond and Zikry, 2018 provided insights on competition between transgranular and intergranular crack path in polycrystalline aggregates, however they did not analyze the effects on overall fracture toughness.

In this study, a two-dimensional (2D) computational framework that explicitly tracks crack propagation through microstructure with randomly oriented grains is developed. To focus on the effects of GB behavior without complications from the effects of crystallographic texture, a finite deformation isotropic elasticity formualtion and a finite deformation incremental rate-independent plasticity flow formulation with isotropic hardening are assumed for the randomly oriented grains. Within this setting, the grain orientations are only reflected in the GB misorientation angle. A misorientation-dependent interfacial law is assumed for the GBs. This relatively simplistic approach allows the study to focus on the evolution of fracture toughness with the GB structure and behavior. Additionally, this framework allows the competition between transgranular and intergranular ductile fracture to be systematically studied. The analyses carried out focus on quantifying fracture measures in terms of K_{IC}, J_{IC}, and crack growth resistance curves as functions of microstructural attributes. Multiple statistically equivalent microstructure sample sets (SEMSS) are generated and used to assess the stochasticity in the macroscopic fracture toughness due to material microstructural heterogeneity variations. The statistical analyses facilitate the development of semi-empirical models that establish fracture toughness as function of microstructural attributes. Although the material of focus here is Mo, the framework and the model can be used for other materials as well.

2. Framework of analysis

2.1. Computational configuration

Since the pioneering work of Xu and Needleman, 1994, the cohesive finite element method (CFEM) has been extensively used in many applications, including modelling debonding, arbitrary crack propagation through different microstructural constituents, and phase boundaries (Xu and Needleman, 1996; Zhai et al., 2004; Tomar et al., 2004; Li and Zhou, 2013a). The primary aim here is to quantitatively relate fracture toughness to microstructural attributes and the competition between different fracture mechanisms. To achieve this, it is necessary to explictly resolve microstructure level fracture processses. Following Li and Zhou, 2018, we adopt the CFEM to explicitly track transgranular and intergranular crack propagation in fully dense microstructures with grains and grain boundaries. The 2D multiscale CFEM computational configuration is shown in Fig. 1. A 2D compact tension specimen is used to simulate laboratory-scale fracture toughness tests. The configuration meets all requirements of the ASTM standard (Standard, 2001) for plane strain fracture toughness and J-integral measurements. The overall dimensions of the CT specimen are 6.12 mm $\times$ 6 mm. The microstructure region is 2.5 mm $\times$ 2.5 mm in size and is inserted around the tip of the pre-crack of 2.25 mm in length. The CFEM is implemented in the microstructure region
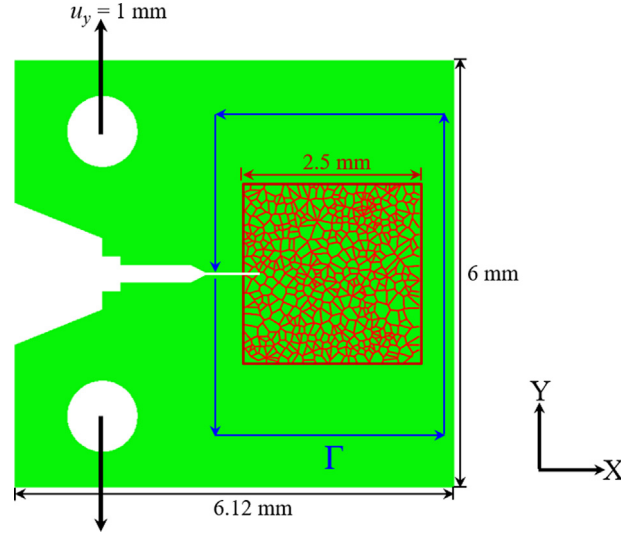
Fig. 1. Multiscale computational framework for prediction of fracture toughness of ductile metals with microstructures.

which is stitched to the homogeneous section using a mesh-tie constraint, just as in Li and Zhou, 2013a. The size of the microstructure region is so chosen such that the plastic zone is fully within this region. Overall mode-I loading is effected through an imposed load point displacement, as indicated in the Fig. 1. The rigid body motion of the load point along the Y direction is kinematically coupled with the surface of the hole through the general multiple point constraint (MPC) in ABAQUS. The edges of the specimen are traction-free and conditions of plane strain prevail.

2.2. Material and microstructure

In order to account for the effect of grain orientations and the GB characteristics on the fracture of ductile materials with grain structures, single phase pure molybdenum (Mo) is chosen due to the existence of significant experimental data (Lim and Watanabe, 1989; Lim and Watanabe, 1990; Watanabe, 1993, 1994, 2011). Specifically, the data for unalloyed Mo (Watanabe, 2011) show that GB fracture strength exhibits a near sinusoidal variation with the grain boundary misorientation angle. GBs with misorientation angles below 15° or above 75° are nearly as strong as the grains, but GBs with misorientation angles in the range of 15° - 75° can have strengths as low as half of that of the grains. These low fracture strength GBs are the likely sites for crack initiation and propagation. The microstructures are generated using the Voronoi tessellation function. Four levels of grain size (measured in terms of the mean grain intercept length) are considered. To quantify the stochasticity in fracture behavior due to variations in microstructure morphology, twenty statistically similar instantiations of microstructure for each grain size are used. Fig. 2 shows four representative instantiations from each of the four statistically equivalent microstructure sample sets (SEMSS). In all cases, the grains are randomly orientated. A set of Euler angles is used to specify the 3D orientation of each grain with respect to the specimen axes as indicated in Fig. 1. The grain orientations in Fig. 2 are denoted by the plane of the grains that is parallel to the specimen plane (X-Y) using the scheme of plane colors in the stereographic projections of the crystallographic plane normals on an inverse pole figure map (Nolze and Hielscher, 2016). Due to the cubic crystalline symmetry, the stereographic triangle contains all possible grain orientation relations, as shown in the figure. Although the color map does not uniquely define the orientation of the grains, it indicates that no orientation is preferred in the microstructure, i.e. the grains are indeed randomly oriented. The mean intercept grain size for each of the SEMSS are shown in Fig. 3(a). The error bars account for statistical variations among the twenty instantiations in each set. Due to the random orientations of the grains, GBs are associated with a range of misorientation angles. Since fracture strength is a function of the GB misorientation angle (Watanabe, 2011), the GB misorientation angle is calculated. This angle is the angle by which one grain is to be rotated about an axis common to the contacting grain pair in order to bring the grains into coincidence. The Euler angle sets are used to calculate the orientation matrix (g) for all grains. This matrix is

$$g = \begin{bmatrix} \cos\Phi_1\cos\Phi_2 - \sin\Phi_1\sin\Phi_2\cos\Phi & \sin\Phi_1\cos\Phi_2 + \cos\Phi_1\sin\Phi_2\cos\Phi & \sin\Phi_2\sin\Phi \\ -\cos\Phi_1\sin\Phi_2 - \sin\Phi_1\cos\Phi_2\cos\Phi & -\sin\Phi_1\sin\Phi_2 + \cos\Phi_1\cos\Phi_2\cos\Phi & \cos\Phi_2\sin\Phi \\ \sin\Phi_1\sin\Phi & -\cos\Phi_1\sin\Phi & \cos\Phi \end{bmatrix}. \quad (1)$$

It facilitates calculation of the misorientation matrix (Δg) at the GBs using

$$\Delta g = g_1 . g_2^{-1}, \quad (2)$$
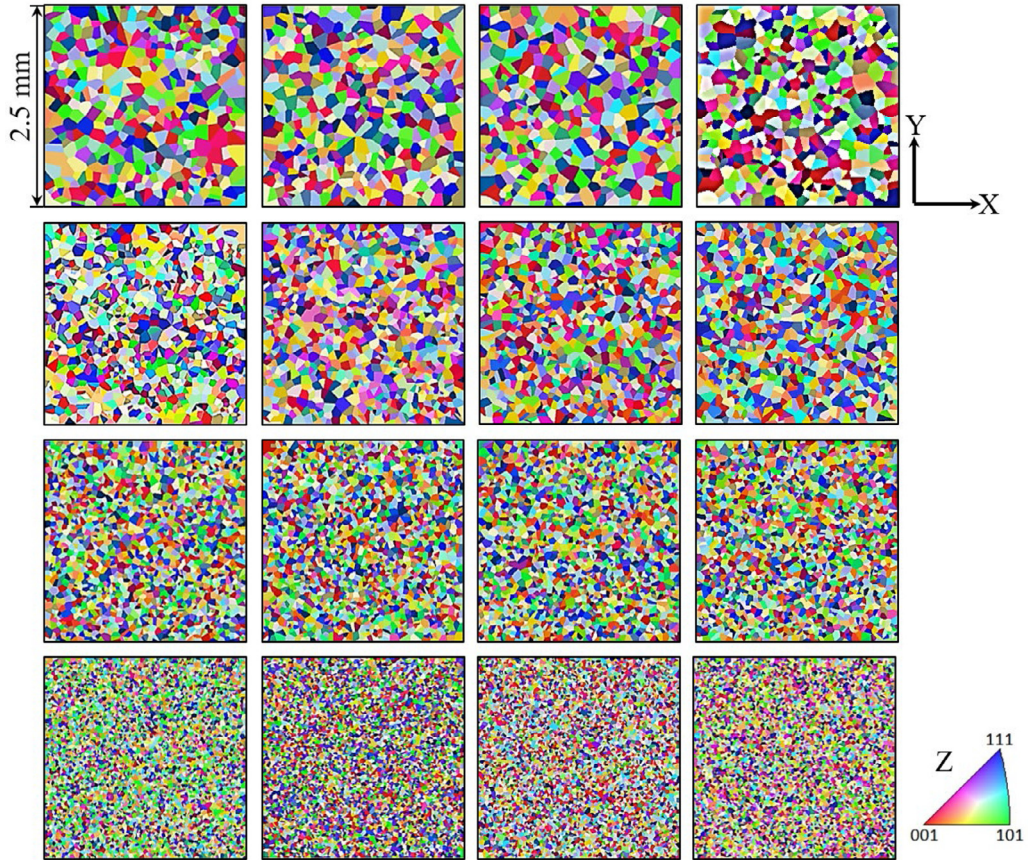
Fig. 2. Four out of twenty instantiations of microstructure from each of the four statistically equivalent microstructure sample sets (SEMSS). The colors in the stereographic triangle indicate the crystalline plane normals of grains parallel to the Z axis of the specimen in Fig. 1.
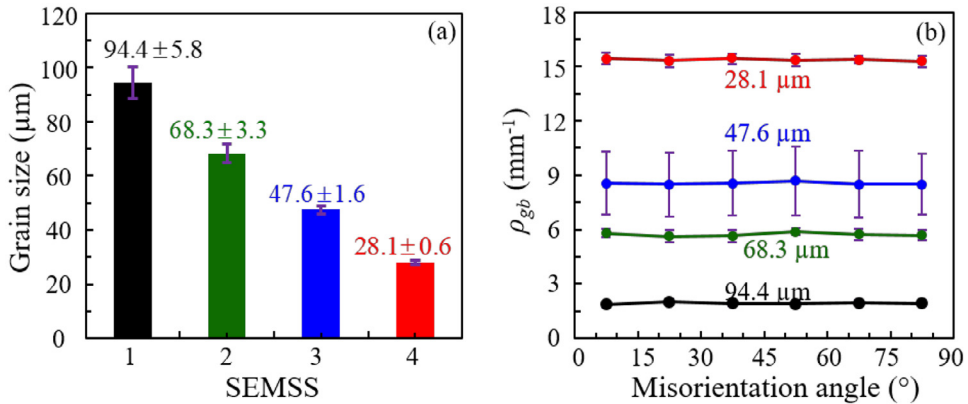
Fig. 3. (a) Mean intercept grain sizes and (b) grain boundary density as functions of misorientation angle for all four sets of statistically equivalent microstructure sample sets (SEMSS).

where g_1 and g_2 are the orientation matrices of two neighboring grains. The misorientation angle (θ) is then calculated using the trace of the misorientation matrix via

$$\cos\theta = \frac{1}{2}[trace(\Delta g)].$$

(3)

The axis of misorientation can be calculated using the off-diagonal terms of the misorientation matrices. Since our focus is on resolving the fracture behavior of GBs as a function of their misorientation angles, the misorientation axes are not
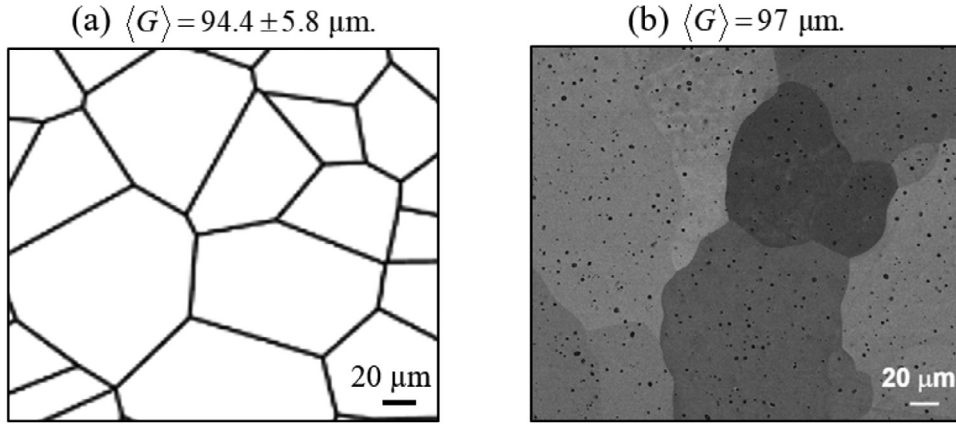
Fig. 4. (a) Computationally generated polycrystalline microstructure, (b) optical micrograph of an unalloyed Mo (Sturm et al., 2007). Image used with permission.

shown. Fig. 3(b) shows the density of GBs at different misorientation angles. The GB density (ρ_{gb}) is defined as

$$\rho_{gb} = \frac{L_{gb}}{A_m}, \tag{4}$$

where L_{gb} is the total length of GBs at a given misorientation angle, and A_m denotes the area of the microstructure region. The GBs with misorientation angles in the range of 15°-75° are the fracture prone sites in a polycrystalline material and are hence called the weaker GBs with an associated density of ρ_{gb}^W. Fig. 4 compares a computationally generated microstructure with an experimentally obtained microstructure obtained by Sturm *et al.* who reported the mechanical properties of unalloyed Mo having an average grain size of 97 μm (Sturm et al., 2007). The grain structure of this Mo is very similar to the computationally generated microstructure with an average grain size of 94.36 ± 5.76 μm.

2.3. Material models

Our primary intent is to delineate the effects of grain boundary characteristics on crack path, and subsequently quantify the relative contributions of intergranular and transgranular crack propagation to the overall fracture resistance. To focus on GB misorientation angles and GB strength on the fracture toughness, we use a simplified model in which the effect of anisotropy in the bulk grain behavior is ignored. As a first attempt, this simplified treatment, although having limitations, offers a setting that allows the GB effects to be highlighted. More comprehensive models can and should be developed in the future. In our setting, the random grain orientations allow the misorientation angles to be evaluated. A bilinear isotropic elastic-plastic constitutive law is adopted for the grains. A misorientation-dependent interfacial law is formulated for the grain boundaries.

The grains and the homogenized section outside the microstructure region follow a rate independent elasto-plastic constitutive law with isotropic hardening under the large strain assumption. An incremental theory of plasticity is used. The Jaumann rate of Kirchhoff stress ($\dot{\tau}$) evolves with the conjugate rate of deformation tensor (**D**) following

$$\dot{\tau} = \mathbf{L} : (\mathbf{D} - \mathbf{D}^p), \tag{5}$$

where **L** represents the tensor of elastic moduli. For isotropic elastic response,

$$\mathbf{L} = 2\mu\tilde{\mathbf{I}} + \lambda\mathbf{I} \otimes \mathbf{I}, \tag{6}$$

where,

$$\lambda = \frac{E\nu}{(1+\nu)(1-2\nu)}, \text{and} \mu = \frac{E}{2(1+\nu)}. \tag{7}$$

In the above relations, E represents the Young's modulus and ν the Poisson's ratio. We assume associative decomposition of the rate of deformation tensor into an elastic part and a plastic part, i.e.,

$$\mathbf{D} = \mathbf{D}^e + \mathbf{D}^p. \tag{8}$$

The plastic part of **D** varies with the deviatoric part of the Kirchhoff stress following,

$$\left.\begin{array}{l} \mathbf{D}^p = \frac{3\dot{\bar{\varepsilon}}^p}{2\bar{\sigma}}\boldsymbol{\tau}', \text{ where,} \\[2mm] \bar{\sigma} = \sqrt{\frac{3}{2}\boldsymbol{\tau}':\boldsymbol{\tau}'}, \text{ and} \\[2mm] \dot{\bar{\varepsilon}}^p = \frac{1}{k}\left\langle \frac{3\boldsymbol{\tau}'}{2\bar{\sigma}} : \dot{\tau} \right\rangle \frac{3\boldsymbol{\tau}'}{2\bar{\sigma}}. \end{array}\right\} \tag{9}$$
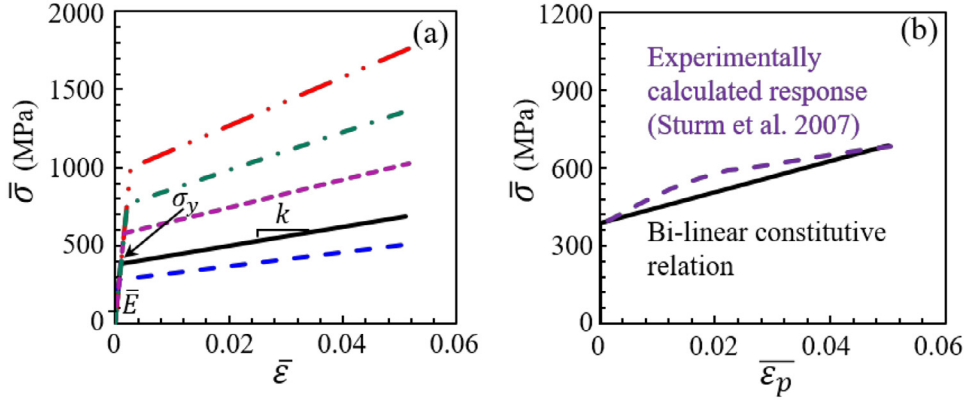
Fig. 5. (a) Bi-linear elastic-plastic constitutive relations for Mo at different yield stress levels, (b) comparison of the bi-linear material model with experimentally determined stress-strain response of Mo.

Here, $\bar{\sigma}$ is the Mises equivalent stress and $\dot{\bar{\varepsilon}}^p$ is the equivalent plastic strain rate which takes non-zero values only after yielding. The material follows the Mises flow rule with isotropic hardening characterized by k in the above equation. The constitutive relation used is the linear stress-strain relation under uniaxial loading in the form of

$$\bar{\sigma} = \sigma_y + k\bar{\varepsilon}^p, \tag{10}$$

where, σ_y is the yield stress from uniaxial tensile test and k represents the strain hardening effect. The values of these parameters are taken from Sturm et al., 2007. The solid black line in Fig. 5(a) shows the equivalent stress-strain relation for Mo. The dotted lines correspond to the other four levels of yield strength considered for the purpose of parametrically exploring the effect of the yield stress. The rate of strain hardening remains the same in all five cases. Fig. 5(b) shows a comparison of the baseline bilinear stress-strain model and the experimentally obtained stress-strain response of unalloyed Mo (Sturm et al., 2007).

To model arbitrary crack propagation through the grains and GBs, cohesive elements are inserted along all element boundaries within the microstructure region. The cohesive elements follow a bilinear traction separation law. In this model, the traction applied on any cohesive surface (**t**) is work conjugate to the interfacial separation (**δ**). The uncoupled traction-separation constitutive relation can be written as,

$$\mathbf{t} = \begin{Bmatrix} t_n \\ t_s \end{Bmatrix} = (1 - D) \begin{bmatrix} K_{nn} & 0 \\ 0 & K_{ss} \end{bmatrix} \begin{Bmatrix} \delta_n \\ \delta_s \end{Bmatrix}, \tag{11}$$

where $t_n = \mathbf{n} \cdot \mathbf{t}$, $t_s = \mathbf{s} \cdot \mathbf{t}$, $\delta_n = \mathbf{n} \cdot \boldsymbol{\delta}$, and $\delta_s = \mathbf{s} \cdot \boldsymbol{\delta}$ are the normal and tangential components of **t** and **δ**, respectively, and **n** and **s** are the unit vectors normal and tangential to the cohesive surface, respectively. **K** represents the stiffness tensor connecting **t** and **δ** before damage sets in. D represents a scalar damage variable. $D = 0$ until damage initiates. Damage sets in when the following criterion is satisfied.

$$\left. \begin{array}{l} \left\{ \left(\frac{t_n}{t_n^{\max}}\right)^2 + \left(\frac{t_s}{t_s^{\max}}\right)^2 \right\}^{1/2} = 1, \ with \\ t_n^{\max} = t_s^{\max} = T_{\max}. \end{array} \right\} \tag{12}$$

Since the normal and tangential strengths are taken to be the same and denoted as $T_{\max}$ partly owing to the lack of detailed experimental information, the damage initiation criterion can simply be written as,

$$\frac{t}{T_{\max}} = \left\{ \frac{t_n^2 + t_s^2}{T_{\max}^2} \right\}^{1/2} = 1. \tag{13}$$

In the above relation, t is the effective traction. When the effective separation ($\delta_m = \sqrt{\delta_n^2 + \delta_s^2}$) reaches a value of δ_m^0, damage initiates, as shown in Fig. 6(a). Before damage initiates, the separation is completely reversible, i.e., upon unloading and reloading, traction follows the same path AB as shown in the figure. As a result, no energy is dissipated and $D = 0$. Beyond point B where $\delta = \delta_m^0$, the interfacial strength and stiffness begin to degrade and, upon unloading, the traction follows the path CA, dissipation occurs, and D is calculated as,

$$D = \frac{\delta_m^c \left(\delta_m^{\max} - \delta_m^0 \right)}{\delta_m^{\max} \left(\delta_m^c - \delta_m^0 \right)}. \tag{14}$$

In the above relation, $\delta_m^{\max}$ represents the hitherto maximum value of the effective separation attained during the loading history up to the current time (i.e., unloading does not affect this value). This treatment allows successive unloading and
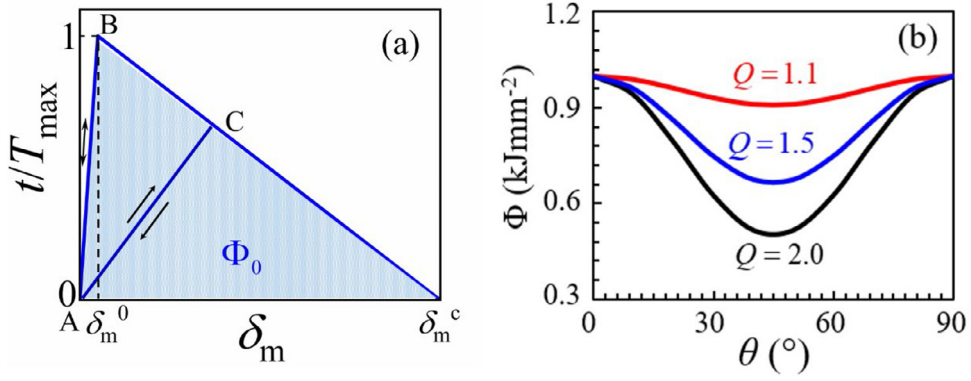
Fig. 6. (a) Bi-linear traction-separation relation for the cohesive crack faces, (b) variation of the cohesive energy with grain boundary misorientation angle.

Table 1
Interfacial parameters.

Q	K_{nn} (MPa)	$(\Phi_0)_{max}$(kJ/mm^2)	T_G(MPa)	T_{GB}^{min}(MPa)
1.1	500×10^6	1	962.5	875
1.5	500×10^6	1	962.5	641.67
2.0	500×10^6	1	962.5	481.25

reloading with progressively weakening interfacial strength and stiffness represented by evolving point C and line CA to be tracked and implemented. Upon reloading, the traction follows the path AC with the stiffness reduced by the factor of $(1\text{-}D)$ relative to that embodied in line AB. The interfacial strength and stiffness vanish upon full separation when the effective separation reaches $\delta_m = \delta_m^c$, with $D = 1$ and dissipation reaching Φ_0. The limiting value of $D = 1$ corresponds to complete separation. Note that

$$\frac{1}{2} \cdot T_{\max} \cdot \delta_m^c = \Phi_0. \tag{15}$$

For the GBs, the cohesive parameters are functions of the misorientation angle, i.e.,

$$\left.\begin{array}{l} \Phi = \Phi(T_{\max}, \delta_m^c), \\ T_{\max} = T_{\max}(\theta). \end{array}\right\} \tag{16}$$

Experiments (Watanabe, 2011) showed that the fracture strength of GB first decreases and then increases with increasing angle of misorientation between adjacent grains. The fracture strength is the lowest for GBs with misorientation angles in the range of $15° - 75°$. Fracture strength increases beyond $75°$ and GBs with misorientation angles around $90°$ are nearly as strongly as grains. Therefore, we assume a sinusoidal function of the form

$$\left.\begin{array}{l} T_{GB}(\theta) = C_1 + C_2 \cos(4\theta), \\ C_1 = \frac{1}{2}\left(T_{GB}^{max} + T_{GB}^{min}\right), \\ C_2 = \frac{1}{2}\left(T_{GB}^{max} - T_{GB}^{min}\right). \end{array}\right\} \tag{17}$$

to approximate the variation of the interfacial strength with the GB misorientation angle. In the above relations, $T_{GB}(\theta)$ is the misorientation angle dependent $T_{\max}$ as in Eq. (16) with the subscript "max" omitted for brevity and to avoid confusion. T_{GB}^{max} and T_{GB}^{min} represent the maximum and minimum values of T_{GB}, respectively. The maximum value T_{GB}^{max} is taken as the cohesive strength of the grains ($T_{GB}^{max} = T_G$). Fig. 6(b) shows profiles of T_{GB} for different values of T_{GB}^{min} while T_G is kept constant. These cases can be distinguished by the ratio $Q = T_G/T_{GB}^{min}$, which represents the degree of variation of $T_{GB}(\theta)$ as the GB misorientation angle changes. The values of the cohesive parameters used are shown in Table 1. The maximum cohesive energy used in this model scales with the fracture toughness of pure Mo. The range of misorientation-dependent variation of T_{GB} is obtained from experimental data (Watanabe, 2011). Further calibration of the cohesive parameters is described in the next section. Following the convergence criterion described in (Tomar et al., 2004), the lower bound of the cohesive finite element size is estimated as

$$d_z \geq \frac{\lambda_o \delta_{sc}}{T_{\max}} \frac{\bar{E}}{(1 - \bar{\nu}^2)} \frac{\sqrt{2} + 1}{1 - \bar{\nu}} = 0.006 \mu\text{m}, \tag{18}$$

whereas the upper bound is

$$d_z \leq \frac{9\pi}{32} \frac{\bar{E}}{(1 - \bar{\nu}^2)} \frac{\Phi_o}{T_{\max}^2} = 360 \mu\text{m}. \tag{19}$$
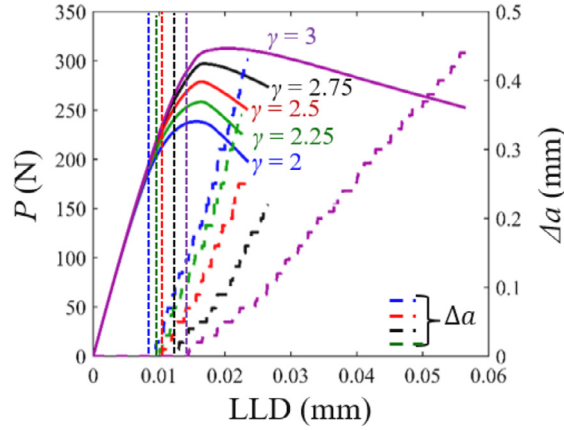
Fig. 7. Load (P) -Load line displacement (LLD) - crack extension (Δa) relations obtained from numerical simulations for five levels of the ratio (γ) between interfacial strength and grain yield strength for homogeneous Mo without microstructure.

The element size of 5 μm used falls well within this range and also sufficiently resolves the grain structure. The 3-node 2D plane strain CPE3 elements are used for the bulk material, and the 4-node 2D standard COH2D4 cohesive elements are used for the interfaces. A quasi-static implicit scheme with Newton's algorithm is used in ABAQUS/Standard to solve the problem.

2.4. Model calibration and evaluation of fracture toughness

The ASTM standard (Standard, 2001) calls for the fracture toughness to be calculated from the load (P) vs load line displacement (LLD) curve for a CT specimen. This curve is calculated in the simulations along with the plastic zone size at the growing crack tip. To calibrate the model parameters, multiple calculations are performed at different levels of relative strength values between the GBs and the grains as indicated by the ratio between the GB strength and the yield strength of the material

$$\gamma = \frac{T_G}{\sigma_y}. \tag{20}$$

Initially, the interfacial strength ratios are so chosen that significant cracking occurs before plasticity in the bulk material sets in. At very high values of γ, crack tip blunting occurs instead of crack propagation with constrained plasticity close to the tip. So, to begin with, a range of γ values that lead to considerable cracking are chosen. For calibration, a homogeneous specimen without microstructure is used. Cohesive elements are placed along all the element boundaries as well to model fracture in this homogeneous case. The P vs LLD curves are plotted for five cases along with the crack extension (Δa) in Fig. 7. Higher load levels are seen as the normalized interfacial strength (γ) increases. The rate of crack propagation decreases as γ increases. Fig. 8 shows the evolution of the plastic zone size ahead of a growing crack. The zone size increases and reaches a steady state and remains constant after a finite amount of crack extension. Higher values of γ correspond to faster attainment of the steady state. Constant plastic zone size signifies steady state crack growth and a constant dissipation rate per unit crack length growth. In the analysis, steady crack propagation over up to 0.8 mm or at least 10-12 grains even for the largest grain size is analyzed. This crack propagation length is well within the microstructure region (2.5 × 2.5 mm) and conditions in the microstructure region are free from the specimen boundary effects.

For K_{IC} to be calculated from the P vs LLD plots, the specimen dimensions should satisfy

$$a, (W - a) \geq 8r_p, \tag{21}$$

where, a and W are projected length of the growing crack and the width of the specimen (5 mm in our case), respectively. This condition may not be satisfied due to the relatively smaller specimen size. Instead, we calculate K_{IC} via the J-integral using paths through the homogeneous region outside the microstructure region. The J-integral is (Rice, 1968)

$$\left.\begin{array}{l} J = \int_\Gamma \left(wdy - \boldsymbol{T} \cdot \frac{\partial \boldsymbol{u}}{\partial x} ds\right), \\ w = \int_0^{E_{ij}} \boldsymbol{\tau} : d\mathbf{E}, \\ E_{ij} = \frac{1}{2}\left(F_{ki}F_{kj} - \delta_{ij}\right). \end{array}\right\} \tag{22}$$

$\boldsymbol{T}$ is the traction on a surface with normal $\mathbf{n}$ in the reference configuration, $\boldsymbol{u}$ is the displacement, $\boldsymbol{\tau}$ is the Kirchoff stress, $\mathbf{E}$ is the Lagrangian strain measure conjugate to $\boldsymbol{\tau}$, and $\mathbf{F}$ is the deformation gradient. Γ is the path along which the integral is calculated, as indicated in Fig. 1. Fig. 9 shows J as a function of crack extension for five different levels of γ for
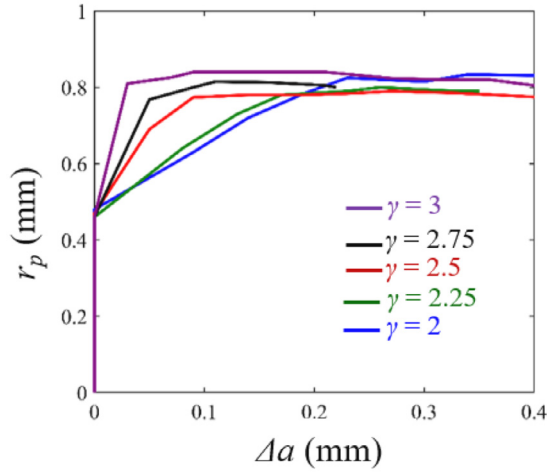
Fig. 8. Evolution of the plastic zone size (rp) as crack growth occurs at five levels of the ratio (γ) between interfacial strength and grain yield strength for homogeneous Mo without microstructure.
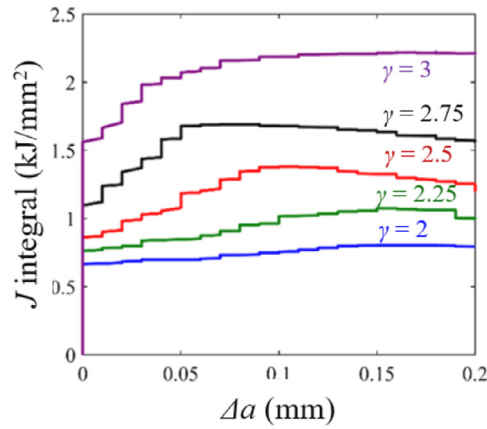
Fig. 9. Variation of J-integral with crack extension (Δa) at five levels of the ratio (γ) between interfacial strength and grain yield strength for homogeneous elastic-plastic Mo without microstructure.

the homogeneous isotropic elastic-plastic material response. The J value at crack initiation is denoted as J_i and the value corresponding to the attainment of steady-state is termed as J_{ss}. For J_{IC} calculations to be valid,

$$a, (W - a), b \geq \frac{25J_{ss}}{\sigma_y}. \tag{23}$$

Our specimen configuration satisfies this condition.

The J-integral accounts for energy dissipated through both surface creation and plasticity around the crack tip. J can also be calculated from a single P vs LLD curve using the point of criticality (Rice et al., 1973), i.e.,

$$J = \frac{P\delta_{crack}}{b}\left(1 + 16\beta D^2 \left[\frac{P}{P_{max}}\right]^2\right), \tag{24}$$

where, δ_{crack} is the crack tip opening displacement, and β, D are geometric constants whose values are taken from Rice et al., 1973. Fig. 10 compares the J_i and J_{ss} calculated from Eqs. (22) and (24) for the five levels of the normalized interfacial strength in Fig. 9. The J_i values match, while some differences are seen for J_{ss}. The empirical relation in Eq. (24) tends to overestimate. The difference is larger at lower γ (normalized interfacial strength) values. All J calculations in this paper use the integral in Eq. (22).

Once J_{IC} is calculated, K_{IC} is obtained via

$$K_{IC} = \sqrt{\frac{J_{IC}\bar{E}}{1 - \bar{\nu}^2}}. \tag{25}$$
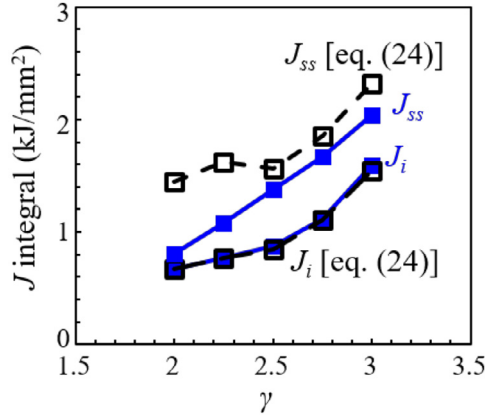
Fig. 10. Comparison of the fracture resistance in terms of J_i and J_{ss} calculated using the area integral with that calculated using the empirical equation proposed by (Rice et al., 1973).
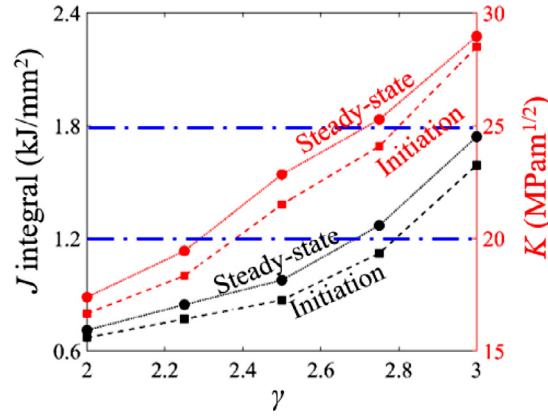
Fig. 11. Fracture toughness in terms of J and K at crack initiation and at attainment of steady-state crack growth over a range of γ.

Fig. 11 shows J_i, J_{IC}, K_i, and K_{IC} for different levels of γ. As the normalized interfacial strength increases, the fracture toughness increases. The experimentally determined fracture toughness for pure Mo with a grain size of 97 µm is 24.2 ± 2.3 MPa$\sqrt{m}$ (Sturm et al., 2007). The calculated K values fall well within this range for $\gamma = 2.5$. This value of γ is taken for all subsequent calculations.

The J-integral can be decomposed into a surface part and an inelasticity part, i.e.,

$$J = J_S + J_P. \tag{26}$$

The surface part J_S can be easily evaluated and has the dependence form of

$$J_S = \Phi(T_{\max}(\theta), \delta_m^c). \tag{27}$$

Eqs. (26) and (27) allow the plastic dissipation rate J_P to be calculated readily. It is used to quantify the contribution of plasticity to fracture resistance.

2.5. Evaluation of fracture mechanisms

The CFEM based model explicitly tracks the intergranular and transgranular fracture mechanisms. The fractions of the crack path associated with transgranular and intergranular fracture are

$$\left. \begin{aligned} H_g &= \frac{L_g}{L_g + L_{gb}}, \\ H_{gb} &= \frac{L_{gb}}{L_g + L_{gb}}. \end{aligned} \right\} \tag{28}$$

L_g and L_{gb} represent the lengths of crack in each type of fracture sites. The $L = L_g + L_{gb}$ is total crack length. The crack path tortuosity (ξ) is

$$\xi = \frac{L}{a}, \tag{29}$$
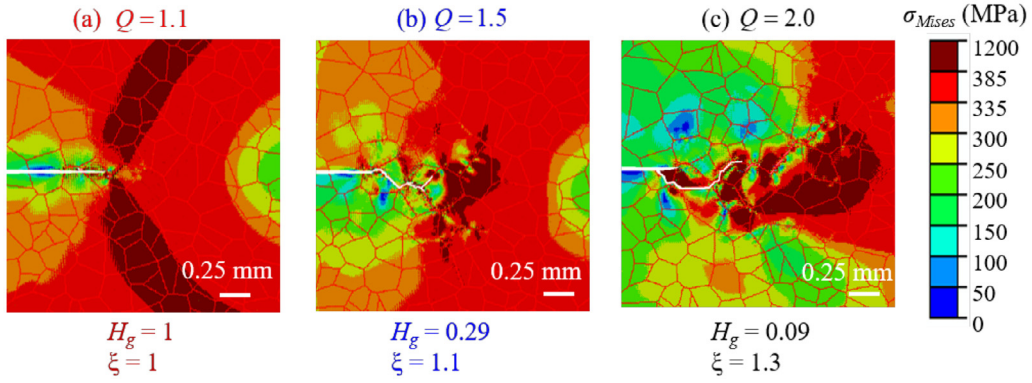
Fig. 12. Crack propagation in a representative microstructure from the SEMSS with ~95 μm grain size for different levels of the ratio between maximum and minimum GB strength. The grain yield strength is 385 MPa in all cases.
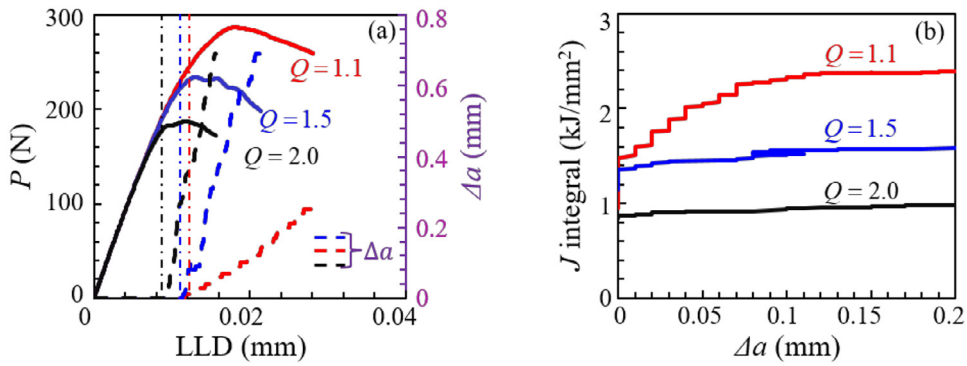
Fig. 13. (a) Variation of load (P) and crack extension (Δa) with load line displacement (LLD), and (b) crack growth resistance curve in terms of J-integral vs crack extension (Δa) for different levels of the ratio between maximum and minimum GB strength. The grain yield strength is 385 MPa in all cases. The SEMSS with ~95 μm grain size is used.

where a is the projected crack length in the overall direction of propagation. J_S can be expressed in terms of the crack path descriptors as

$$J_S(H, \xi, \Phi) = \xi\left(H_g \Phi_g + H_{gb} \Phi_{gb}(\theta)\right). \tag{30}$$

In the above relation, Φ_g and Φ_{gb} are, respectively, the work of separation for the grains and the GBs as defined in Eq. (15). The multiple instantiations of statistically similar microstructures in the SEMSS are used to account for the stochasticity in fracture behavior and fracture toughness.

3. Results and discussion

The results of the microstructure based CFEM calculations, the subsequent fracture toughness characterization, and analyses are discussed in this section. All samples in the SEMSS are subjected to the same loading. Systematic comparisons of the fracture trends and the mechanisms and are made in terms of K_{IC}, J_{IC}, H, and ξ.

3.1. Effect of GB fracture strength

To explore the effect of GB fracture strength, three sets of simulations are performed using three different GB strength profiles characterized by three different Q values (Fig. 6(b)). The grain yield strength is the same (385 MPa) for the three cases. Figs. 12–14 show the results obtained using the SEMSS with a mean grain size of ~95 μm.

Fig. 12 shows the stress distributions and crack profiles of one sample in the SEMSS at the three different cases of GB fracture strength. As Q (the ratio between the maximum and minimum GB strengths) increases, the crack path becomes more tortuous and tends to meander through weaker GB sites. The intergranular fracture is predominant at the higher Q values (Fig. 13(b) and (c)), as indicated by the H and ξ values. Fig. 13(a) shows the load vs load line displacement curves along with the crack extension for the cases. As the GBs weaken, the crack initiation occurs earlier and the rate of crack propagation increases. The J vs crack extension profiles or crack growth resistance curve Fig. 13(b) corroborate the trend. The crack growth resistance increases as the GBs strengthen. The K_i and K_{IC} values obtained from the J_i and J_{IC} values are
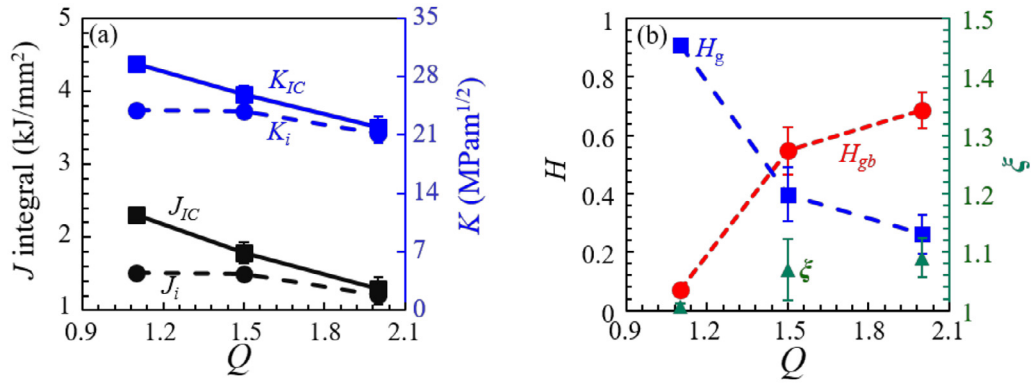
Fig. 14. (a) Fracture resistance in terms of J_i, J_{IC}, K_i, and K_{IC} over a range of Q (ratio between maximum GB strength and minimum GB strength), and (b) fractions of crack lengths inside grains and along grain boundaries, and the crack path tortuosity (ξ) over a range of Q. The grain yield strength is 385 MPa in all cases, and the SEMSS with ~95 μm grain size is used.
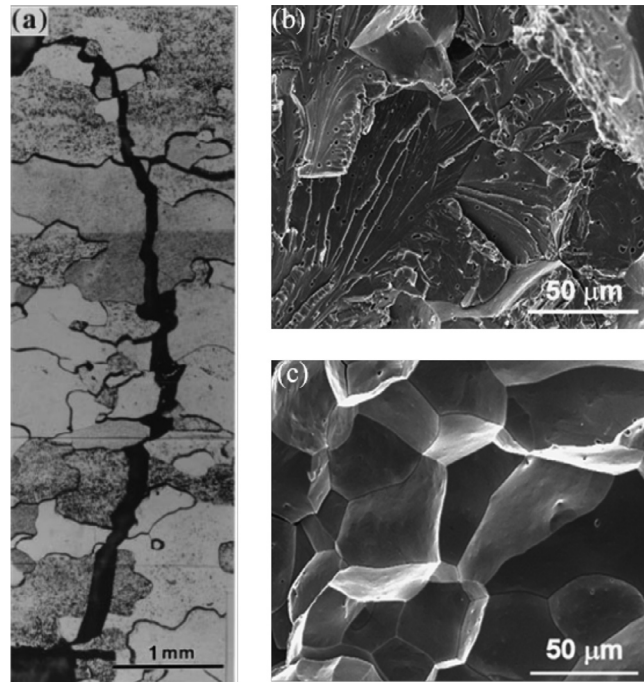
Fig. 15. (a) Crack path in polycrystalline Mo (Watanabe, 2011), (b) transgranular crack propagation in unalloyed Mo, and (c) intergranular crack propagation in a Mo-0.5%Si alloy (Sturm et al., 2007). Reproduced with permission.

shown in Fig. 14(a). For the material with the strongest GBs (Q=1.1), the K_{IC} lies in the range of 29.4 – 29.6 MPa$\sqrt{}$m. For the material with GBs having intermediate strength (Q=1.5), K_{IC} lies in the range of 24.8 – 26.8 MPa$\sqrt{}$m. For the material having the weakest GBs (Q=2.0), K_{IC} ranges from 20.7 – 23.3 MPa$\sqrt{}$m. The experimentally obtained value of K_{IC} for unalloyed Mo with a grain size of ~97 μm is 21.9-26.5 MPa$\sqrt{}$m (Sturm et al., 2007). Therefore, the K_{IC} values calculated using the weaker GBs ($Q \in [1.5, 2]$) are in agreement with the experimental values. Fig. 15(b) can be used to analyze the different fracture mechanisms operative at different GB strength levels. Pure mode-I straight transgranular crack propagation dominates when the GBs are nearly as strong as the grains (Q=1.1, Fig. 13(a)). As the GBs become weaker (Q increases), intergranular crack propagation starts to dominate. Also, the transgranular cracks preferentially propagate through interfaces perpendicular to the loading direction in a mode I fashion. The same trends are observed in all samples in the statistically equivalent microstructure sample set (SEMSS), with the fluctuations among the samples in the set indicated by the error bars. In the process, the crack path tortuosity ξ increases and approaches a plateau as Q increases beyond 1.5. The experimentally obtained fractographs for pure Mo with randomly oriented grains indicate that both intergranular and transgranular fracture mechanisms are operative (Fig. 15). Sturm et al. report that the addition of Si renders the GBs more brittle, resulting in dominance of intergranular fracture as shown in Fig. 15(c). This observation matches with the case of the weakest GB strength
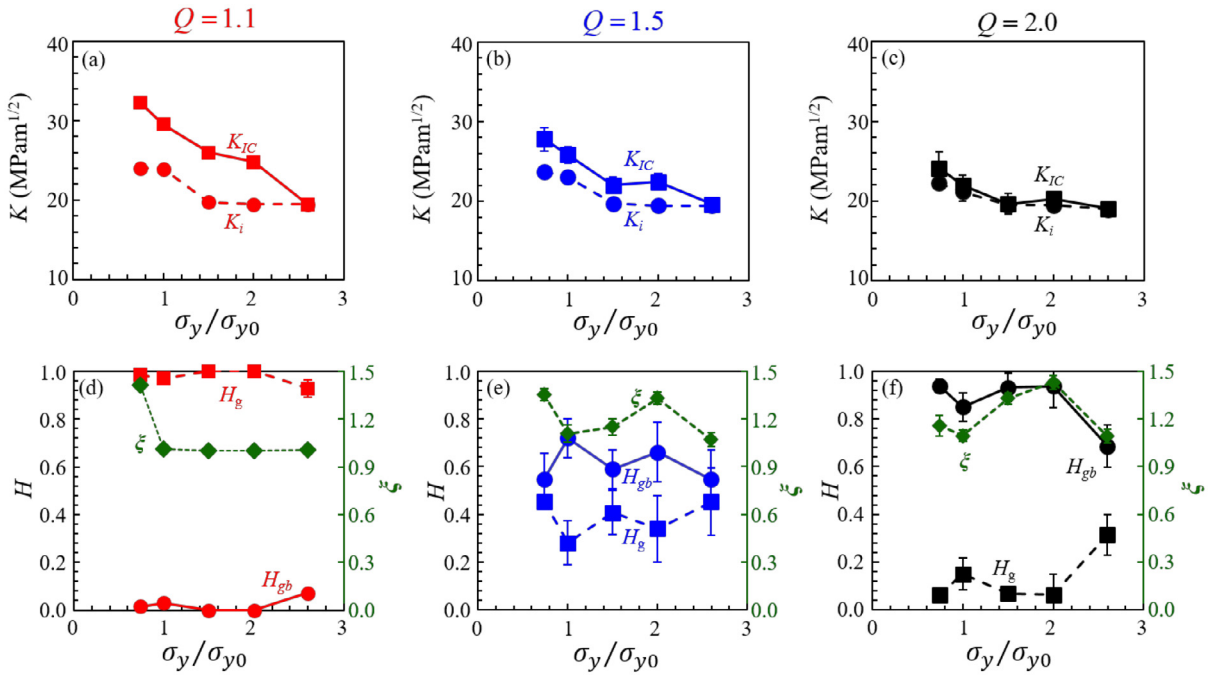
Fig. 16. (a)-(c) Variations of K_i and K_{IC} and (d)-(f) variations of the crack length fractions and crack path tortuosity with normalized grain yield strength at different levels of the ratio between maximum and minimum GB strengths. The SEMSS with ~95 μm grain size is used.

profile($Q = 2$). Thus, the simulations with weaker GBs are in agreement with the experimental observations in terms of both the fracture toughness value and the fracture micromechanisms.

3.2. Competition between crack formation and plasticity

In order to analyze the effect of constituent plasticity on the fracture mechanisms, four other levels of grain yield strength ($\sigma_y = 285, 578, 770, 1000$ MPa) are considered. Three sets of calculations with different GB strength profiles are performed using the SEMSS for the ~95 μm grain size at all levels of the grain yield strength mentioned above. Fig. 16 shows the overall fracture toughness in terms of both K_i and K_{IC} as a function of the yield strength normalized with the yield strength of the base material case ($\sigma_{y0} = 385$ MPa). The error bars indicate stochastic variation among samples in the SEMSS. The toughening effect of plasticity on fracture toughness values is more pronounced when the GBs are nearly as strong as the grain fracture strength. The amount of increase in crack growth resistance from initiation to steady state propagation decreases as the GB strength ratio increases. For $Q = 1.1$, Fig. 16(d) shows that the transgranular crack propagation prevails at all levels of grain plasticity. At the highest level of grain plasticity, crack initiates along the planes of maximum shear and as a result the crack path tortuosity is higher. Both crack path tortuosity and plasticity contribute to the enhancement of the overall fracture toughness. The effect is more clearly seen in the steady state fracture toughness (K_{IC}) than in the initiation fracture toughness (K_i). For $Q = 1.5$, Fig. 16(e) shows that both intergranular and transgranular fracture are operative. At the highest level of grain plasticity, the higher value of crack path tortuosity is a consequence of both intergranular fracture and transgranular fracture through interfaces of maximum shear. The co-operative interplay of crack path tortuosity and plasticity promoted by the transgranular crack propagation results in the highest fracture toughness values. As the grain plasticity level decreases, intergranular fracture dominates over transgranular fracture. Even though intergranular fracture results in a tortuous crack path, the overall fracture toughness decreases due to the suppression of plastic dissipation caused by a lower fraction of transgranular crack propagation. At the lowest value of grain plasticity, again, intergranular and transgranular fracture contribute nearly equally to the overall crack path. However, the crack primarily propagates in a mode-I fashion, resulting in the toughening effect of crack path tortuosity and plasticity both negligible. In the absence of both toughening mechanisms, the fracture toughness is the lowest. For $Q = 2$, Fig. 16(f) shows that intergranular crack propagation prevails at all levels of grain plasticity. Even at the highest level of plasticity, plastic dissipation is extremely low because the crack tends to propagate through weaker GBs. High crack path tortuosity results are seen in cases in which intergranular fracture dominates. This is partly due to the fact that a homogeneous grain constitutive model is used. This again leads to the highest fracture toughness. As grain plasticity decreases below a certain point ($\sigma_y/\sigma_{y0} \geq 1.4$), plastic dissipation becomes essentially negligible, and crack path tortuosity is the only remaining toughening mechanism. As a result, the fracture toughness values remain almost the same, independent of grain plasticity.
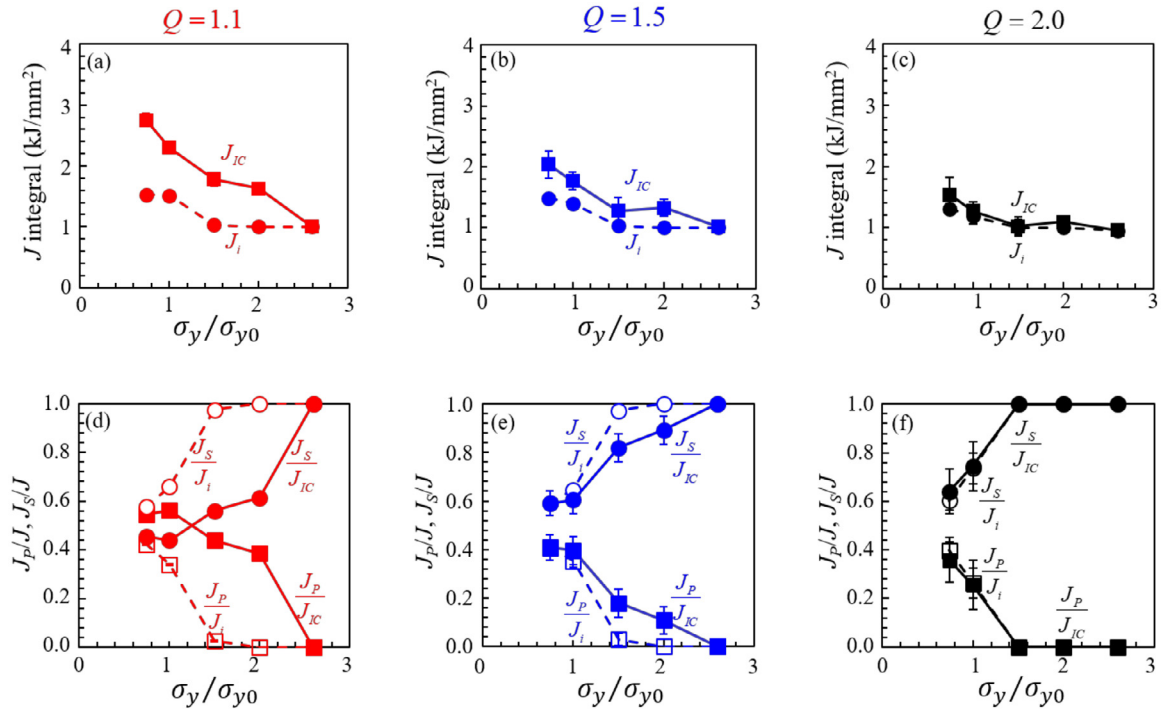
Fig. 17. (a) – (c) J_i and J_{IC}, and (d) – (f) relative contributions of plasticity and surface energy release rate to the fracture resistance for different levels of normalized grain yield strength. The SEMSS of ~95 μm grain size is used.

3.3. Competition between surface energy release and plastic dissipation

The same sets of simulations carried out using different grain yield strength levels and different GB strength profiles are considered here to delineate the competition between plastic dissipation and surface energy release rate. Again, the SEMSS has an average grain size of ~95 μm. Fig. 17 shows the relative contributions of plastic dissipation and surface energy release rate to J_i and J_{IC}. The error bars denote statistical variations among samples in the SEMSS. At the onset of crack propagation, surface energy release accounts more for the initiation fracture resistance than plasticity at all levels of GB strength. For $Q = 1.1$, plasticity contributes more than the surface creation to the steady state fracture resistance for $\sigma_y/\sigma_{y0} \leq 1.35$. As the grain plasticity decreases, surface energy tends to dominate the fracture behavior, resulting in lower overall fracture toughness. For $Q = 1.5$, surface energy always contributes more than plasticity to the overall fracture toughness. The fracture toughness is the highest when the contributions from surface creation and plasticity are balanced. For $Q = 2$, plastic dissipation has a significant effect only at low yield stress levels, as for $\sigma_y/\sigma_{y0} \geq 1.5$ the fracture toughness is completely determined by surface energy dissipation. For the toughening effect of plasticity to be more pronounced, the mismatch between grain and GB fracture strengths should be low. As the surface energy along the GBs decreases, the crack preferentially goes through the GBs, suppressing plastic dissipation even when the grain yield stress is low. At lower levels of plasticity (higher grain yield stress), the surface energy term dominates and the fracture toughness ceases to depend on the grain yield strength.

3.4. Effect of microstructural attributes on fracture

To establish relations between the macroscale fracture behavior and microstructure, four SEMSS with different levels of mean intercept grain size are considered. For each SEMSS, three GB strength profiles are used. The grain yield strength is kept the same at 385 MPa for all cases. Fig. 18(a)-(d) show the crack paths in one representative microstructure from each of the four SEMSS. Fig. 19 shows K_i, K_{IC}, J_i, J_{IC}, relative contributions of plastic dissipation and surface energy release in terms of J_s/J_{IC}, J_p/J_{IC}, and the crack path descriptors H and ξ, all as functions of the grain size. Over the range analyzed, grain size and GB density do not have a significant influence on the fracture initiation resistance J_i and K_i. However, these attributes indeed have a significant influence on the steady state fracture toughness measures K_{IC} and J_{IC}. The fracture toughness is the highest when the grain size is 50-70 μm. At the finest grain size (~25 μm), intergranular crack propagation dominates, resulting in the highest crack path tortuosity. Consequently, plastic dissipation is suppressed and crack meandering is the only toughening mechanism. The corresponding fracture toughness is approximately 20% below the highest level seen for a grain size of ~70 μm. As the grain size increases to ~50-70 μm, transgranular fracture occurs in higher proportions. As
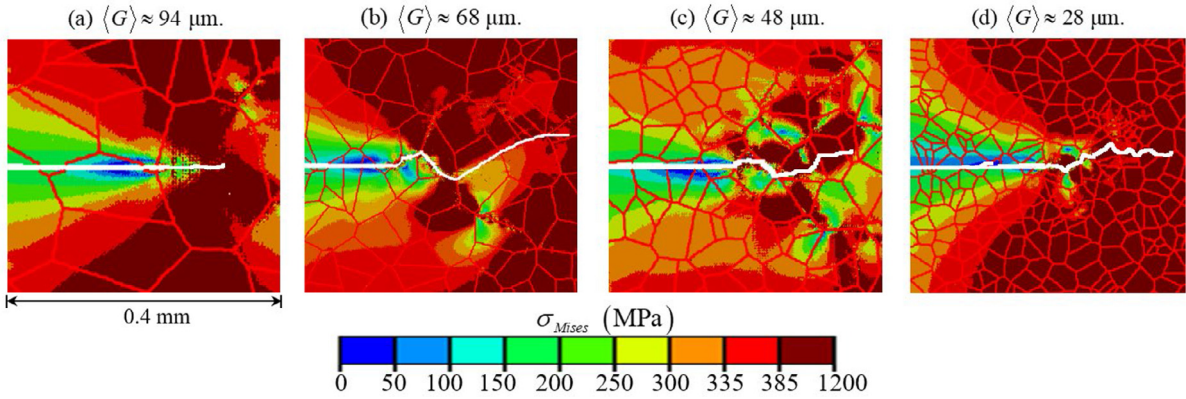
Fig. 18. Crack propagation at different grain sizes. One sample from each of the four SEMSS with different grain sizes is used. The grain yield strength is 385 MPa, and the GB strength profile correspond to $Q = 1.5$.
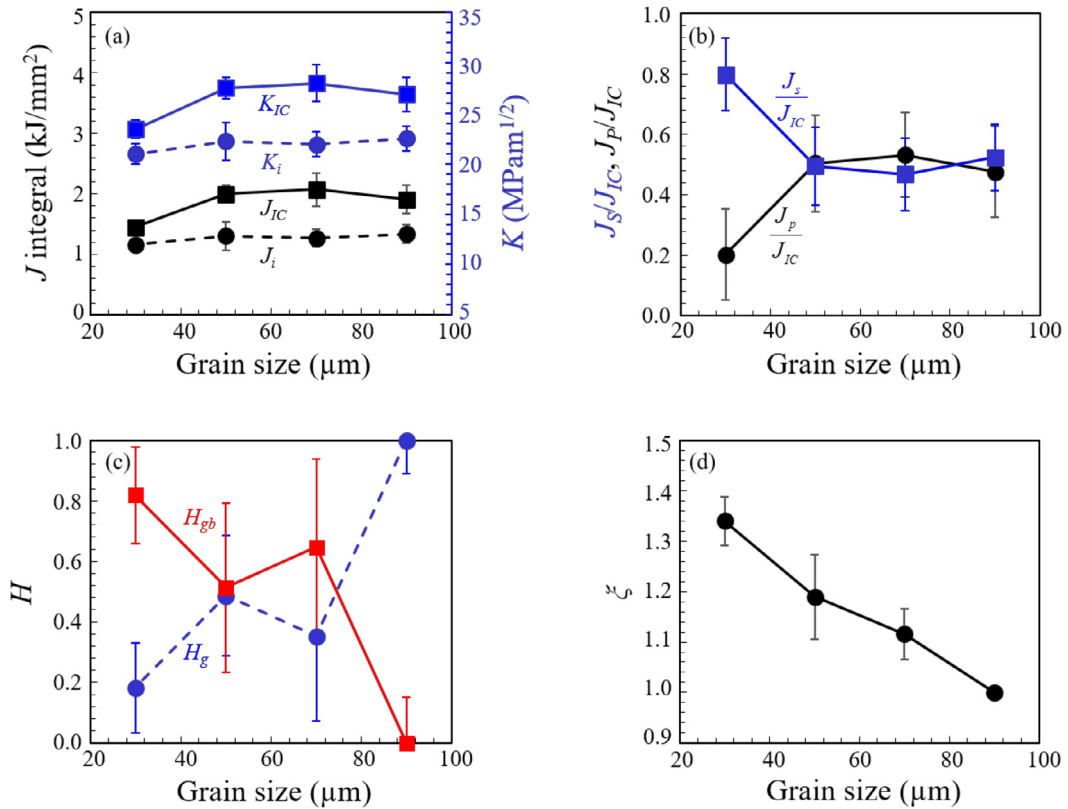
Fig. 19. (a) The fracture toughness measures, (b) relative contribution of plasticity and surface energy to fracture resistance, (c) the crack propagation mechanisms in terms of the crack path fractions, and (d) the crack path tortuosity, as function of the mean intercept grain sizes. The grain yield strength is 385 MPa, and the GB strength profile correspond to $Q = 1.5$ in all cases.

a result, both plastic dissipation and crack path tortuosity act as toughening mechanism. A tortuous crack path arises not only due to the intergranular fracture, but also due to transgranular fracture along directions of maximum shear. Therefore, the material shows higher fracture toughness values. The contributions of surface energy and plasticity are nearly the same towards the overall energy dissipation for these intermediate levels of grain size. As the grains become even coarser (~ 100 μm), transgranular crack propagation begins to dominate and intergranular fracture is almost negligible. Transgranular fracture occurs primarily through mode-I direction and hence the crack path tortuosity is also insignificant. In this extreme case, plasticity is the only toughening mechanism and therefore, the material exhibits a slightly reduced fracture toughness value.
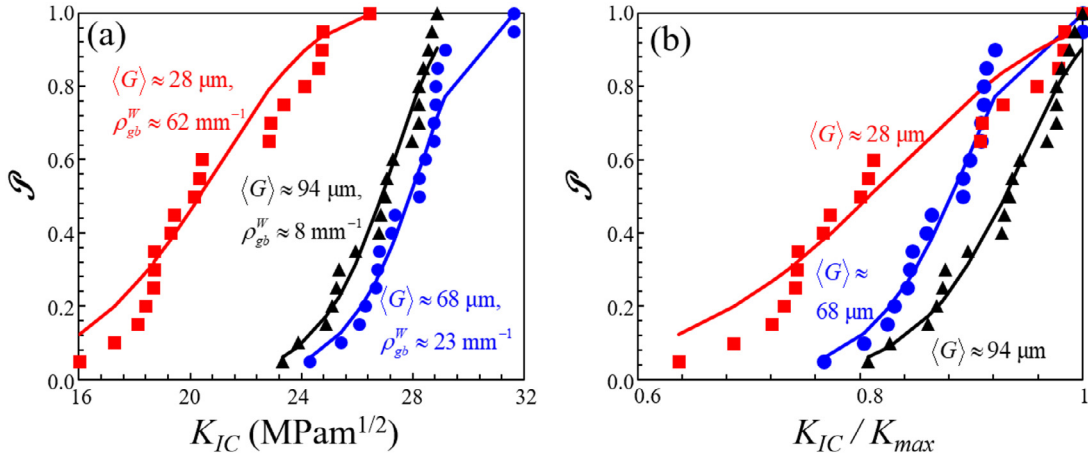
Fig. 20. Cumulative probability of fracture as function of (a) fracture toughness, and (b) normalized fracture toughness K_{IC}/K_{max}. The symbols represent calculated results and the lines represent fits to the Weibull distribution. The grain yield strength is 385 MPa and GB strength profile corresponds to $Q = 1.5$.

The grain size dependence of ductile fracture toughness varies from one material to the other. Some studies exist that attempt to capture a specific trend between the grain size and the fracture toughness (Fan, 1995; Ahadi and Sun, 2016; Molkeri et al., 2019). Experimental studies on different material systems show that three types of trend could be found. (1) K_{IC} increases with decreasing grain size as is observed in Ti, Al based alloys, (2) K_{IC} is barely dependent on grain size like in α-Fe, and (3) K_{IC} decreases with decreasing grain size as exhibited by Cu-Zn, Cu-Ni, and NiTi alloys. Molkeri et al., 2019 showed that fracture resistance of ductile material decreases with decreasing mean grain size. In our case K_{IC} first increases slightly with decreasing grain size and then decreases with decreasing grain size. The trend depends upon the relative contributions of plasticity and new surface creation to the overall fracture resistance. In this case, the contribution of plasticity associated with transgranular crack propagation in the coarse grained microstructure wins over the contribution of crack path tortuosity associated primarily with intergranular crack propagation in the fine grained microstructure.

The interplay between transgranular and intergranular crack growth with constituent plasticity via crack path tortuosity explains the observation that fracture toughness is the highest at coarser grain sizes in the 50-70 µm range. As the grain size decreases, the mean free path for transgranular crack propagation decreases and the probability of intergranular crack propagation increases. Therefore, for a microstructure with fine grains (~30 µm), intergranular crack propagation dominates, causing an overall reduction in fracture resistance. For microstructures with 70-90 µm grains, comparable amounts of transgranular and intergranular crack propagation takes place. The higher mean free paths for transgranular crack propagation also contribute to maintaining constituent plastic dissipation.

3.5. Stochasticity in fracture

Variations at the microstructure level result in considerable scatter in fracture toughness values and is a primary source of material behavior stochasticity at the macroscopic scale. An analysis is carried out using the results for $\sigma_y = 385$ MPa, $Q = 1.5$, and the four SEMSS. Each set consists of 20 statistically similar samples. The two-parameter Weibull distribution function is used to quantify the probability of observing a particular fracture toughness value

$$P(K = K_{IC}) = 1 - \exp\left[-\left(\frac{K_{IC}}{K_0}\right)^{m_f}\right], \tag{31}$$

where, K_0 and m_f represent the normalization factor and the shape factor, respectively. The normalization factor (K_0) can also be interpreted as the value of fracture toughness with a 63% probability. It can be used as a characteristic fracture toughness value. Fig. 20 shows the probability distribution for three grain sizes. The result for the 48 µm grain size is not shown for graphical clarity since it is very close to the results for the 95 and 68 µm grain sizes. The distribution is the widest for the smallest grain size which has the highest density of weaker GBs. Since all bulk and interfacial properties are taken as deterministic here, the stochastic variations are fully attributable to the microstructural variations.

To relate the stochasticity in fracture toughness to GB behavior, the probability distribution of fracture toughness at three values of Q are shown in Fig. 21. The lines are fits to Eq. (31). The SEMSS with the ~95 µm grain size is used along with a yield strength of 385 MPa. Scatter is lowest at $Q = 1.1$ and increases as Q increases, suggesting that GB strength variations is a significant source of the stochasticity in fracture behavior.
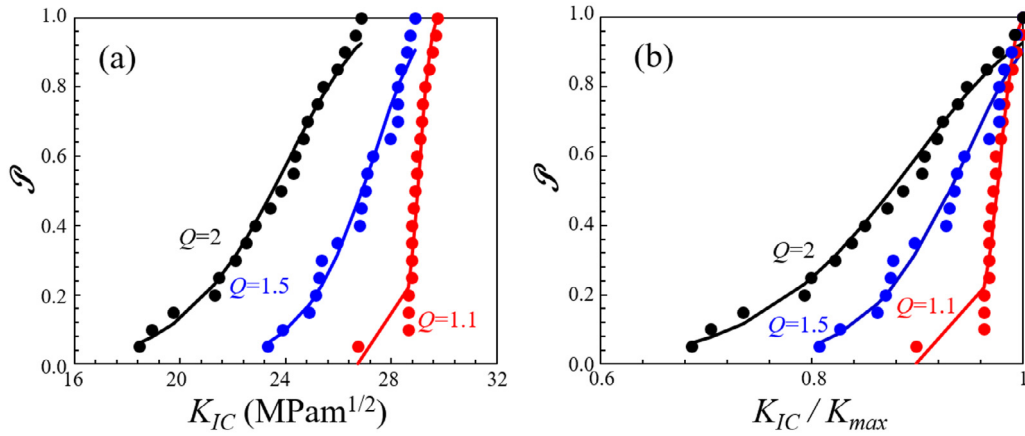
Fig. 21. Cumulative probability of fracture as function of (a) fracture toughness, and (b) normalized fracture toughness K_{IC}/K_{max} for three different GB strength profiles. The symbols represent calculated results and the lines represent fits to the Weibull distribution. The grain yield strength is 385 MPa and the SEMSS with ~95 μm grain size is used.
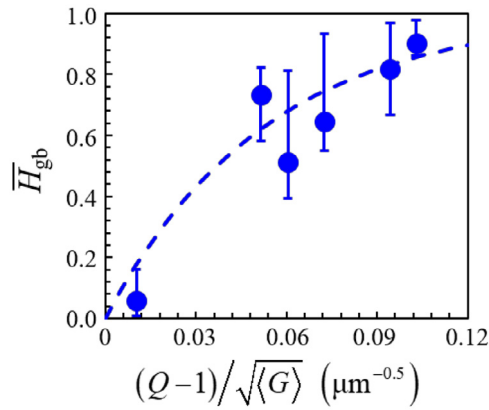
Fig. 22. Fraction of intergranular crack length as a function of the microstructure characterized by the parameter $(Q-1)/\sqrt{\langle G \rangle}$ in μm$^{-0.5}$. The dash line represents fit to Eq. (33). The grain yield strength is 385 MPa in all cases.

3.6. Characterization of fracture toughness

To delineate the trend of fracture toughness variation with microstructural attributes and GB behavior, contributions of grain boundary energy and plasticity are assessed as functions of the grain size and the GB strength profiles. To this end, the grain size and the grain boundary strength profiles are varied while the grain yield strength is kept at 385 MPa. The grain size and the GB strength profiles directly influence the fracture mechanisms. H_{gb} increases as Q increases (i.e., as overall GB strength decreases) and as the mean intercept grain size decreases. The combined effects of Q and $<G>$ can be characterized by

$$H_{gb} = 1 - \exp\left[-\frac{D(Q-1)}{\sqrt{\langle G \rangle}}\right], \tag{32}$$

where, $<G>$ is in μm, and D is a fitting parameter in μm. $D = 18.34$ μm when the grain yield strength is at 385 MPa. It is to be noted that the lowest value possible for Q is 1 which corresponds to uniform boundary strength. Fig. 22 shows the trend revealed by calculations. The form of the equation satisfies the limiting conditions, i.e., (a) when $Q = 1$, the material is homogeneous without microstructure (as the highest GB strength is the same as the fracture strength inside the grains), and hence $H_{gb} = 0$; (b) when $<G>$ tends to 0, the microstructure has extremely fine grains with negligible mean free path for transgranular fracture, and hence $H_{gb} = 1$.

The surface part of the energy release rate J_S can be evaluated using Eqs. (32) and (30) for each crack path (each sample) as a function of grain size and GB strength profile. For each material case (each SEMSS), the mean value of J_S can be
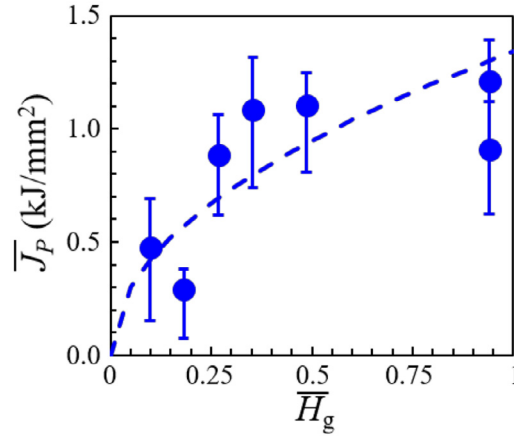
Fig. 23. Mean plastic part of the energy release rate as a function of the transgranular crack path ratio. The dash line represents fit to Eq. (35). The grain yield strength is 385 MPa.
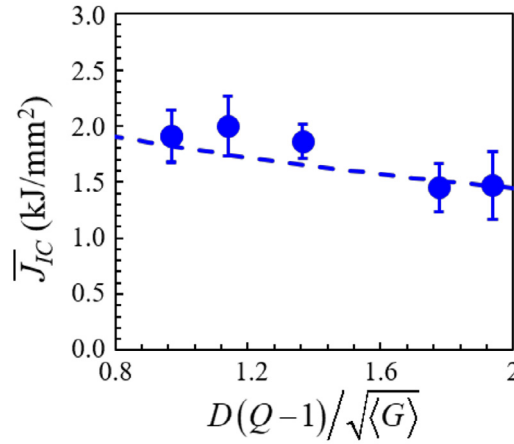
Fig. 24. $\bar{J}_{IC}$ as a function of microstructure as characterized by the dimensionless parameter $D(Q-1)/\sqrt{\langle G \rangle}$. The dash line represents the mean relation in Eq. (37). The grain yield strength is 385 MPa.

expressed as a function of the mean crack path tortuosity ($\bar{\xi}$) and the mean GB energy ($\bar{\Phi}_{gb}$), i.e.,

$$\bar{J}_S = \bar{\xi}\left[\bar{\Phi}_{gb} + \left(\Phi_g - \bar{\Phi}_{gb}\right)\exp\left\{-\frac{D(Q-1)}{\sqrt{\langle G \rangle}}\right\}\right], \tag{33}$$

where, Φ_g, Φ_{gb}, and J_S are in kJ/mm^2. As expected, when $Q = 1$, $\bar{J}_S = \bar{\xi}\Phi_g = \bar{J}_S^g$, which is the surface part of the energy release rate for a uniform material without microstructure. On the other hand, when $\langle G \rangle \to 0$, $H_{gb} \to 1$, and $\bar{J}_S \to \bar{\xi}\bar{\Phi}_{gb} \to \bar{J}_S^{gb}$, which is the average surface energy release rate due to GBs only.

To assess the plastic part of the energy release rate, J_P is plotted as a function of the transgranular crack path ratio in Fig. 23. The relation can be described by

$$J_P = J_P^g\sqrt{H_g} = J_P^g\sqrt{1 - H_{gb}}, \tag{34}$$

where, J_P^g is the plastic part of the energy release rate for a homogeneous material without GB and is measured in kJ/mm^2. When $H_g = 1$, the material is homogeneous, $H_{gb} = 0$, and $J_P = J_P^g$. $J_P^g = 1.34$ kJ/mm^2 at the grain yield strength of 385 MPa. For each material case (SEMSS), Eqs (32) and (34) allow the mean value of J_P to be obtained as a function of grain size and GB strength profile as

$$\bar{J}_P = J_P^g\exp\left\{-\frac{D(Q-1)}{2\sqrt{\langle G \rangle}}\right\}. \tag{35}$$

Finally, the mean value for J_{IC} can be obtained as a function of the mean grain size and the GB strength profile by combining Eqs. (33) and (35). The relation is given by

$$\bar{J}_{IC} = \bar{J}_S^{gb} + \left(\bar{J}_S^g - \bar{J}_S^{gb} \right) \exp \left[-\frac{D(Q-1)}{\sqrt{\langle G \rangle}} \right] + J_P^g \exp \left[-\frac{D(Q-1)}{2\sqrt{\langle G \rangle}} \right]. \tag{36}$$

Again as expected, when $Q = 1$, $\bar{J}_{IC} = \bar{J}_S^g + J_P^g$; and when $\langle G \rangle \to 0$, $\bar{J}_{IC} \to \bar{J}_S^{gb}$, the contribution from plasticity becomes negligible. Fig. 24 compares the mean J_{IC} value calculated from Eq. (36) (dash line), with numerical results over a range of values of the characteristic microstructure parameter $D(Q-1)/\sqrt{\langle G \rangle}$. The trend and values are in good overall agreement with each other. This equation captures the overall trend of J_{IC} decreasing with increasing Q and decreasing $<G>$. The relation also shows that the influence of microstructural heterogeneities is more on the surface part of the energy release rate than on the plastic part. Surface energy dominates at higher values of Q (weaker and more inhomogeneous GBs), as well as finer grain sizes.

4. Summary and conclusions

A framework for capturing the interplay between grain boundary structure and constituent plasticity in ductile metals is developed. The framework is used to explore the fracture processes in microstructured metals and relate their fracture toughness to microstructure. The focus is on the effects of grain boundary strength distribution, grain size, and constituent plasticity level as microstructure attributes of interest.

The framework and analysis have yielded significant insights. The contributions include the development of a J-integral based method for predicting the fracture toughness, delineation of the trends in the competition between intergranular and transgranular fracture, and quantification of the tradeoff between microstructure-induced crack tortuosity and constituent plasticity. Using constitutive and interfacial relations calibrated to the properties of Mo, calculations have yielded fracture toughness levels and ranges that are consistent with experimental measurements. Specifically, for unalloyed Mo with a grain size of ~94 μm, the fracture toughness established through the model here is in good agreement with the experimental observations both in terms of fracture toughness and fracture mechanisms. The results allowed the K_{IC} and J_{IC} of Mo to be expressed as functions of microstructural attributes like grain size, grain boundary density, grain boundary fracture strength, and grain yield strength. It is found that transgranular fracture promotes plastic dissipation and thus acts as a toughening mechanism. Grain boundaries with misorientations in the range of 15°-75° have relatively low fracture separation energy, therefore, have a significant detrimental effect on fracture toughness. Lower grain boundaries fracture strength not only directly reduces intergranular dissipation but also inhibits bulk constituent plastic dissipation. As a result, intergranular crack propagation resulting from grain boundary strength variations has competing effects, one is increasing crack path tortuosity which tends to increase grain boundary dissipation, the other is lowering constituent plasticity and limiting grain boundary dissipation due to activation of lower strength boundary sites. The overall arching message is that there is a tradeoff balance between grain boundary strength profile and constituent plasticity level. As such, a proper balance is needed to maximize fracture resistance.

The use of statistically equivalent microstructure sample sets (SEMSS) has allowed the relation between fracture toughness and microstructure to be quantified in a probabilistic manner. This approach recognizes the fact that microstructure variations is an important source of the stochasticity in macroscopic material behavior.

It is worth noting that the multiscale computational framework based on the cohesive finite element reported here is a simplified first step towards more comprehensive accounts of microstructure-fracture toughness relations for ductile polycrystalline materials. To simplify and focus the analysis on the competition between grain boundary behavior and bulk plasticity in this first step, we have chosen to use a homogenous and isotropic in-grain constitutive model and grain boundary misorientation angle dependent interfacial separation relation. Although the calculations here are performed on Mo, the approach can be applied to other material systems. Future developments should further advance the capability, including the account for crystalline plasticity and extension from 2D to 3D. This and the future models can allow microstructure-fracture toughness relations to be established and used to design microstructure configurations with desired or tailored fracture behavior. Such analyses can either precede or follow the fabrication and testing of materials in the laboratory. Therefore, they can be viewed as materials design tools.

Declaration of Competing Interest

None.

Acknowledgments

References

Ahadi, A., Sun, Q., 2016. Grain size dependence of fracture toughness and crack-growth resistance of superelastic NiTi. Scr. Mater. 113, 171–175.

Arafin, M.A., Szpunar, J.A., 2010. Modeling of grain boundary character reconstruction and predicting intergranular fracture susceptibility of textured and random polycrystalline materials. Comput. Mater. Sci. 50, 656–665.

Bachurin, D., 2018. Influence of grain boundary misorientation on intergranular fracture of nanocrystalline palladium. Int. J. Fract. 214, 69–78.

Bond, D.M., Zikry, M.A., 2018. Differentiating between intergranular and transgranular fracture in polycrystalline aggregates. J. Mater. Sci. 53, 5786–5798.

Chen, H., Jiao, Y., Liu, Y., 2015. Investigating the microstructural effect on elastic and fracture behavior of polycrystals using a nonlocal lattice particle model. Mater. Sci. Eng. 631, 173–180.

Ebrahimi, M., Balint, D., Sutton, A., Dini, D., 2019. A discrete crack dynamics model of toughening in brittle polycrystalline material by crack deflection. Eng. Fract. Mech. 214, 95–111.

Fan, Z., 1995. The grain size dependence of ductile fracture toughness of polycrystalline metals and alloys. Mater. Sci. Eng. 191, 73–83.

Fullwood, D.T., Niezgoda, S.R., Adams, B.L., Kalidindi, S.R., 2010. Microstructure sensitive design for performance optimization. Prog. Mater Sci. 55, 477–562.

Guo, X., Chang, K., Chen, L., Zhou, M., 2012. Determination of fracture toughness of AZ31 Mg alloy using the cohesive finite element method. Eng. Fract. Mech. 96, 401–415.

Gurson, A.L., 1977. Continuum theory of ductile rupture by void nucleation and growth: part I—yield criteria and flow rules for porous ductile media. J. Eng. Mater. Technol. 99, 2–15.

Hossain, M., Hsueh, C.-J., Bourdin, B., Bhattacharya, K., 2014. Effective toughness of heterogeneous media. J. Mech. Phys. Solids 71, 15–32.

Kobayashi, S., Inomata, T., Kobayashi, H., Tsurekawa, S., Watanabe, T., 2008. Effects of grain boundary-and triple junction-character on intergranular fatigue crack nucleation in polycrystalline aluminum. J. Mater. Sci. 43, 3792–3799.

Li, Y., McDowell, D., Zhou, M., 2014. A multiscale framework for predicting fracture toughness of polycrystalline metals. Mater. Perform. Charact. 3, 157–172.

Li, Y., Zhou, M., 2013a. Prediction of fracture toughness of ceramic composites as function of microstructure: I. Numerical simulations.. J. Mech. Phys. Solids 61, 472–488.

Li, Y., Zhou, M., 2013b. Prediction of fracturess toughness of ceramic composites as function of microstructure: II. Analytical model.. J. Mech. Phys. Solids 61, 489–503.

Li, Y., Zhou, M., 2018. Effect of competing mechanisms on fracture toughness of metals with ductile grain structures. Eng. Fract. Mech. 205, 14–27.

Lim, L., Watanabe, T., 1989. Grain boundary character distribution controlled toughness of polycrystals—a two-dimensional model. Scr. Metall. 23, 489–494.

Lim, L., Watanabe, T., 1990. Fracture toughness and brittle-ductile transition controlled by grain boundary character distribution (GBCD) in polycrystals. Acta Metall. Mater. 38, 2507–2516.

Liu, R., Kumar, A., Chen, Z., Agrawal, A., Sundararaghavan, V., Choudhary, A., 2015. A predictive machine learning approach for microstructure optimization and materials design. Sci. Rep. 5, 11551.

Liu, Y., Zheng, X., Osovski, S., Srivastava, A., 2019. On the micromechanism of inclusion driven ductile fracture and its implications on fracture toughness. J. Mech. Phys. Solids 130, 21–34.

McDowell, D.L., Olson, G.B., 2008. Concurrent Design of Hierarchical Materials and Structures, Scientific Modeling and Simulations. Springer, pp. 207–240.

Molkeri, A., Srivastava, A., Osovski, S., Needleman, A., 2019. Influence of grain size distribution on ductile intergranular crack growth resistance. J. Appl. Mech. 1–11.

Musienko, A., Tatschl, A., Schmidegg, K., Kolednik, O., Pippan, R., Cailletaud, G., 2007. Three-dimensional finite element simulation of a polycrystalline copper specimen. Acta Mater. 55, 4121–4136.

Nolze, G., Hielscher, R., 2016. IPF coloring of crystal orientation data. Preprint Technische Universität Chemnitz.

Olson, G.B., 1997. Computational design of hierarchically structured materials. Science 277, 1237–1242.

Osovski, S., Needleman, A., Srivastava, A., 2019. Intergranular fracture prediction and microstructure design. Int. J. Fract. 216, 135–148.

Osovski, S., Srivastava, A., Williams, J., Needleman, A., 2015. Grain boundary crack growth in metastable titanium β alloys. Acta Mater. 82, 167–178.

Pardoen, T., Hutchinson, J., 2000. An extended model for void growth and coalescence. J. Mech. Phys. Solids 48, 2467–2512.

Prakash, C., Lee, H., Alucozai, M., Tomar, V., 2016. An analysis of the influence of grain boundary strength on microstructure dependent fracture in polycrystalline tungsten. Int. J. Fract. 199, 1–20.

Rice, J., Paris, P., Merkle, J., 1973. Some further results of J-integral analysis and estimates, Progress in flaw growth and fracture toughness testing. ASTM International.

Rice, J.R., 1968. A path independent integral and the approximate analysis of strain concentration by notches and cracks. J. Appl. Mech. 35, 379–386.

Srivastava, A., Osovski, S., Needleman, A., 2017. Engineering the crack path by controlling the microstructure. J. Mech. Phys. Solids 100, 1–20.

Srivastava, A., Ponson, L., Osovski, S., Bouchaud, E., Tvergaard, V., Needleman, A., 2014. Effect of inclusion density on ductile fracture toughness and roughness. J. Mech. Phys. Solids 63, 62–79.

Standard, A., 2001. Standard test method for measurement of fracture toughness. ASTM, pp. 1–46 E1820-01.

Sturm, D., Heilmaier, M., Schneibel, J.H., Jéhanno, P., Skrotzki, B., Saage, H., 2007. The influence of silicon on the strength and fracture toughness of molybdenum. Mater. Sci. Eng. 463, 107–114.

Tomar, V., Zhai, J., Zhou, M., 2004. Bounds for element size in a variable stiffness cohesive finite element model. Int. J. Numer. Methods Eng. 61, 1894–1920.

Tvergaard, V., Needleman, A., 2006. Three dimensional microstructural effects on plane strain ductile crack growth. Int. J. Solids Struct. 43, 6165–6179.

Watanabe, T., 1993. Grain boundary design and control for high temperature materials. Mater. Sci. Eng. 166, 11–28.

Watanabe, T., 1994. The impact of grain boundary character distribution on fracture in polycrystals. Mater. Sci. Eng. 176, 39–49.

Watanabe, T., 2011. Grain boundary engineering: historical perspective and future prospects. J. Mater. Sci. 46, 4095–4115.

Xu, X.-P., Needleman, A., 1996. Numerical simulations of dynamic crack growth along an interface. Int. J. Fract. 74, 289–324.

Zhai, J., Tomar, V., Zhou, M., 2004. Micromechanical simulation of dynamic fracture using the cohesive finite element method. J. Eng. Mater. Technol. 126, 179–191.

Zikry, M., 1992. Failure modes in cubic crystalline materials. ASME-PUBLICATIONS-AD 36 199-199.

Zikry, M.A., Kameda, T., 1998. Inelastic three dimensional high strain-rate dislocation density based analysis of grain-boundary effects and failure modes in ordered intermetallics. Mech. Mater. 28, 93–102.

Zikry, M.A., Kao, M., 1995. Large-scale crystal plasticity computations of microstructural failure modes. Comput. Syst. Eng. 6, 225–240.